International Journal of Microwave and Wireless Technologies

cambridge.org/mrf

Feed assembly development for INCUS 1.6 m mesh reflector antenna

Gaurangi Gupta, Alessio Mancini and Paolo Focardi

Jet Propulsion Laboratory, California Institute of Technology, Pasadena, CA, USA

Research Paper

Cite this article: Gupta G, Mancini A, Focardi P (2025) Feed assembly development for INCUS 1.6 m mesh reflector antenna. *International Journal of Microwave and Wireless Technologies* **17**(5), 784–793. https://doi.org/10.1017/S1759078725000364

Received: 18 September 2024
Revised: 3 March 2025
Accepted: 8 March 2025

Keywords:
additive manufacturing; antenna design; horn antenna; microwave measurements; modelling and measurements; reflector antenna feed; satellite antennas

Corresponding author: Gaurangi Gupta;
Email: gaurangi.gupta@jpl.nasa.gov

Abstract

INCUS (INvestigation of Convective UpdraftS) is a NASA Earth Science mission scheduled to launch in 2026. The goal of the mission is to study in detail how water vapor and droplets move inside tropical storms and thunderstorms and understand their effects on weather and climate models. To carry out this study, the mission will use three almost identical SmallSats, each equipped with a Raincube-heritage Ka-band radar. The deployable mesh reflector antenna is a new 1.6 m design provided by Tendeg, which is fed using a seven-horn feed assembly to generate overlapping secondary beams. This paper discusses the approach used to design and fabricate the feed assembly and presents the measured and calculated RF performance parameters.

Introduction

Rising ocean temperatures, a consequence of climate change, are contributing to more severe and intense storms. As a result, enhancing weather models to better predict the impacts of climate change on weather patterns is becoming increasingly critical. To address this need, NASA has approved an Earth Science mission set to launch in 2026 called INvestigation of Convective UpdraftS (INCUS) [1]. The mission aims at studying the detailed movements of air and water vapor within tropical storms and thunderstorms, focusing specifically on measuring Convective Mass Flux (CMF). CMF dynamics are currently not well understood, and systematic measurements are expected to provide critical insights into this phenomenon.

The INCUS mission will employ three identical SmallSats, each equipped with a Ka-Band radar and a deployable mesh reflector illuminated by seven independent and offset feedhorns with partially overlapping beams. Figure 1 illustrates the layout of the observatory. The subsystems of the observatory include a 1.6m deployable mesh reflector provided by Tendeg and capable of at least 50 dBi of gain [2], a seven-horn feed assembly provided by Jet Propulsion Laboratory (JPL), a Raincube heritage Ka-Band Dynamic Atmospheric Radar (DAR) [3, 4], and a Tempest-D heritage radiometer [5]. The complete instrument is mounted on the Integrated Payload Structure, also designed and provided by Tendeg, and attached directly onto the spacecraft bus. The bus for each of the three observatories is provided by Blue Canyon Technology, while Colorado State University leads the science team of the project.

The satellites will fly on the same orbit at an altitude of 500 km, producing roughly a 3.2 km coverage with each beam as the 3 dB beamwidth is about 0.35°. The first two observatories will be separated by 30 seconds, while the second and the third will be 90 seconds apart [6, 7]. Altogether, these three satellites will be able to generate time-differenced profiles of the radar reflectivity over a 2-minute window. The middle observatory will also carry a microwave radiometer with four channels between 150 GHz and 190 GHz, offering a 500 km swath. Figure 2 shows a view of the three SmallSats flying in formation. Although they fly along the same orbit, their respective ground tracks do not align perfectly due to Earth's rotation, and their tracking time is not simultaneous. By constantly adjusting the across-track pointing of the three satellites during operations, each observatory will collect data from the same seven partially overlapped ground tracks. The antenna feed consists of seven independent horns, which provide the seven ground tracks with a 2/3 overlap of the 3 dB beams in the across-track direction. This provides the required spatial resolution and data redundancy. The overall swath with seven beams each providing 3.2 km coverage is thus about 9 km. Figure 3 shows the footprint of the seven partially overlapping beams sweeping along a common ground track. Multiple beam reflector antennas using feed horn clusters are commonly used in satellite communication payloads to provide the required coverage [8].

In this paper, we will discuss the approach for the design, fabrication, and measurement of the feed assembly. Both structural and RF design aspects that led to improvements in the overall design will be discussed. Measured and calculated data for return loss, insertion loss, and radiation patterns will also be provided. An earlier version of this paper was presented at the 18th European Conference on Antennas and Propagation (EuCAP 2024) and was published in its Proceedings [9].

© Jet Propulsion Laboratory, California Institute of Technology, 2025. Published by Cambridge University Press in association with The European Microwave Association. This is an Open Access article, distributed under the terms of the Creative Commons Attribution licence (http://creativecommons.org/licenses/by/4.0), which permits unrestricted re-use, distribution and reproduction, provided the original article is properly cited.

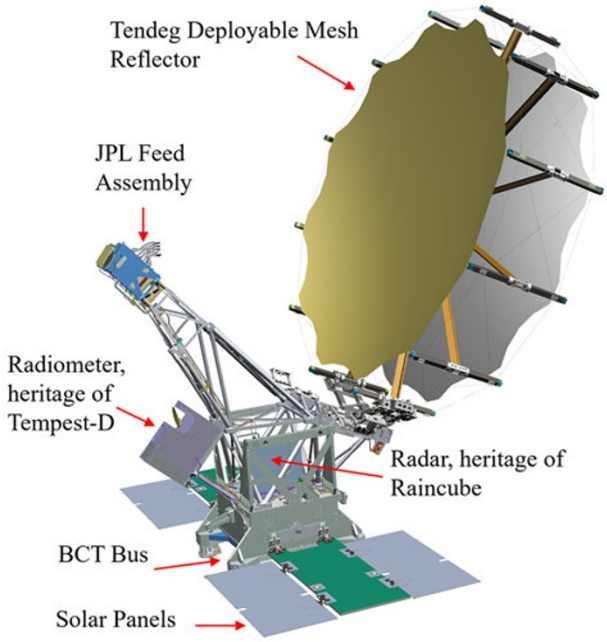


Figure 1. INCUS observatory configuration.

Feed assembly development

The RF performance of the reflector antenna defines the design requirements for the feed assembly. Each SmallSat employed for INCUS features an identical antenna system with a 1.6 m deployable mesh reflector with a focal length over diameter (f/D) ratio of 0.7, and an edge offset of 20 cm. Consequently, the subtended angle from the feed is $\pm$ 34°, and the feed is designed to provide an optimal illumination of the reflector. The reflector optical description is presented in Fig. 4. The reflector antenna is thus designed to obtain 0.35° beamwidth for the secondary radiation patterns. The scan angle in the across-track direction is 0.12° for each adjacent reflector beam. The feed assembly design is based on a flared circular horn with an aperture of 14 mm in diameter and a rectangular-to-circular transition with a WR28 port (l_r = 7.112 mm, w_r = 3.556mm) [10]. The preliminary design of the feed assembly has been presented in previous papers [9, 10, 11, 12]. The interior profile of the horn is shown in Fig. 5, where $l_1 = 1.81$ mm, $l_2 = 11.17$ mm, $l_3 = 7.22$ mm, $d_1 = 14$ mm, $d_2 = 7.96$ mm, $l_4 = 5.89$ mm, $l_5 = 5$ mm. The outer wall of the horn is circularly symmetric with 15.4 mm diameter, where the horn aperture is 14 mm diameter, and lip thickness at the aperture is 0.7 mm.

The initial design and optimization of the single horn was conducted using TICRA CHAMP 3D [13]. A fabrication tolerance analysis was also performed with the latest Uncertainty Quantification feature in TICRA Tools, which confirmed that the horn could be fabricated with the required tolerances while achieving the expected performance. Each horn is designed to operate at 35.755 GHz $\pm$ 11.5 MHz with a return loss better than 30 dB, a peak directivity of 14 dBi, cross-polar isolation of – 30 dB in the broadside direction, and an aperture efficiency of up to 92%. We fabricated a single horn prototype using metal Additive Manufacturing techniques at the JPL, and the measured RF performance closely matched the computed predictions. However, a slight reduction in gain demonstrated the need for better surface accuracy in the fabrication process [11].

The design of the preliminary seven-horn cluster feed assembly is presented in Fig. 5(c). The horn ports are numbered 1 through 7 for easier interpretation of the secondary beams. Ports 1, 3, 4, 5, and 7 are aligned in a straight line with an offset of 14.8 mm in x direction (along-track) and 2.9 mm in y direction (across-track). Ports 2 and 6 have been nested in a Z configuration to provide the required 2/3 beam overlap in the across-track direction. The focal point of the reflector aligns with the phase center of feed 4 of the horn assembly. The rest of the horns are positioned as close as possible to the focus of the reflector while ensuring the required beam overlap and scan performance for the secondary beams. These distances are significantly smaller than the standard flange dimensions for WR28 waveguides, hence, the feeding network has been routed through custom waveguides to connect with the radar interface. These custom waveguides incorporate E-plane bends to expand the gaps between the waveguides, accommodating the standard flange size of 19.05 mm (0.75″), and H-plane bends to align the waveguides into a straight line with 20 mm distance between the ports at the Front-End Switch Assembly (FESA) interface. The FESA is a 1:8 port switch assembly device that routes the radar signal to the seven horns while providing isolation between transmit and receive paths for the radar. The 8th port is used only for testing and then will be terminated into a load during operations.

The effect of bending radii and angles on the return loss for the WR28 waveguides was studied using TICRA Champ and Ansys HFSS. It was concluded that for both E-plane and H-plane bends, a bending radius of 10 mm or more results in a return loss better than 35 dB. After careful assessment of multiple routing configurations, an optimal setup with large bending radii and small bending angles was chosen. Since phase matching between the feed horns is not required to meet mission objectives, varying lengths of the feeding waveguides were acceptable. The H-plane bends have been accommodated in a vertical spacing of $b_1 = 19.17$mm, and the middle E-plane bends have been accommodated in a vertical spacing of $b_2 = 40$mm. Another E-plane bend section is used to tilt the feed cluster by 42° using different bending radii for feeds 1 to 7. The overall size of the feed assembly is approximately 150mm ×150mm × 30mm.

After modelling this preliminary configuration in Ansys HFSS, a CAD model was provided to three different companies for prototyping the assembly. Multiple fabrication approaches were pursued. Figure 6 shows the prototypes of various horn assemblies. Golden Devices, a German start-up company, uses a hybrid additive manufacturing and casting technique to make a prototype with a doubly curved transition between the circular horn and the rectangular WR28 waveguide. The process begins with fabricating a complete Polyimide model using Stereo Lithography Additive (SLA) manufacturing. This model is then plated with copper (or other metals) for intermediate ground testing for the accuracy of the mould. Once the design is finalized, a wax model is then printed and in combination with a gypsum mold is then used to make a solid cast aluminum part all in one piece. The slots all along the side walls of the waveguides are included to facilitate the plating process of the Polyimide parts and also the removal of the wax in the casting process of the aluminum parts. These slots are strategically placed on the waveguide H-wall after optimizing the slot size and distance, thus they don't affect the E-field distribution within the waveguides. A multipaction analysis conducted to assess the impact of these small slots indicates large safety margins for high-power breakdown. The advantage of this manufacturing process is that the waveguide feeding network and the feedhorns can be fabricated as a single piece eliminating the need for intermediate interfaces, fasteners, or alignment pins. This

https://doi.org/10.1017/S1759078725000364 Published online by Cambridge University Press

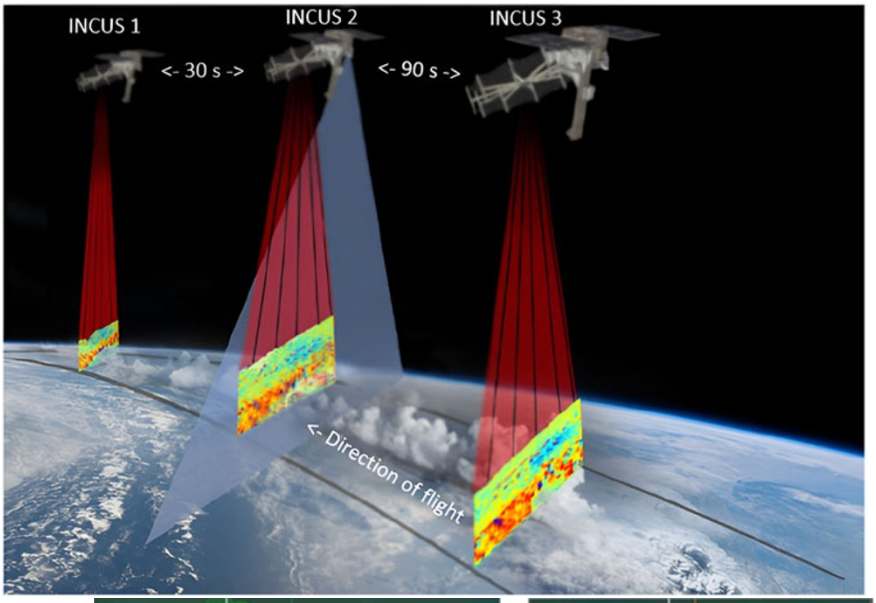


Figure 2. A pictorial representation of the INCUS constellation showing the three observatories and their radar swaths (INCUS1, INCUS2, and INCUS3). INCUS 2 also hosts a radiometer with a swath of 500km.

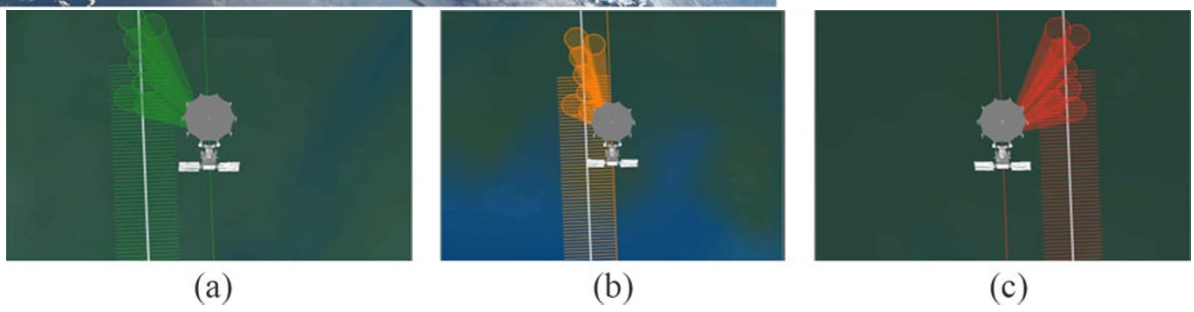


Figure 3. A close-up nadir view of the three smallsats showing the footprint of the seven partially overlapping reflector beams sweeping across a common ground track. Visualization created using satellite orbit analysis program (SOAP) developed by the aerospace corporation. (a) INCUS 1 view, (b) INCUS 2 view, (c) INCUS 3 view.

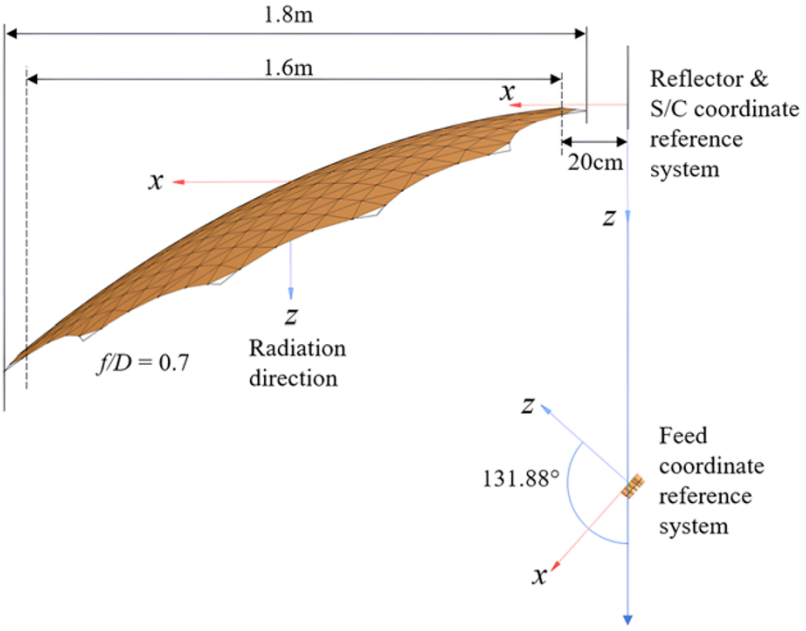


Figure 4. Mesh reflector antenna optical prescription.

integration reduces the mass of the assembly and also allows the fabrication of complex shapes with high surface accuracy which would be impossible to machine in a single piece using standard manufacturing techniques. The overall mass of the feed assembly is 144g. The process utilizes Peraluman30, an alloy of aluminum, for the casting process. The material has slightly lower tensile strength as compared to conventional Al 6061, however, offers similar RF properties.

https://doi.org/10.1017/S1759078725000364 Published online by Cambridge University Press

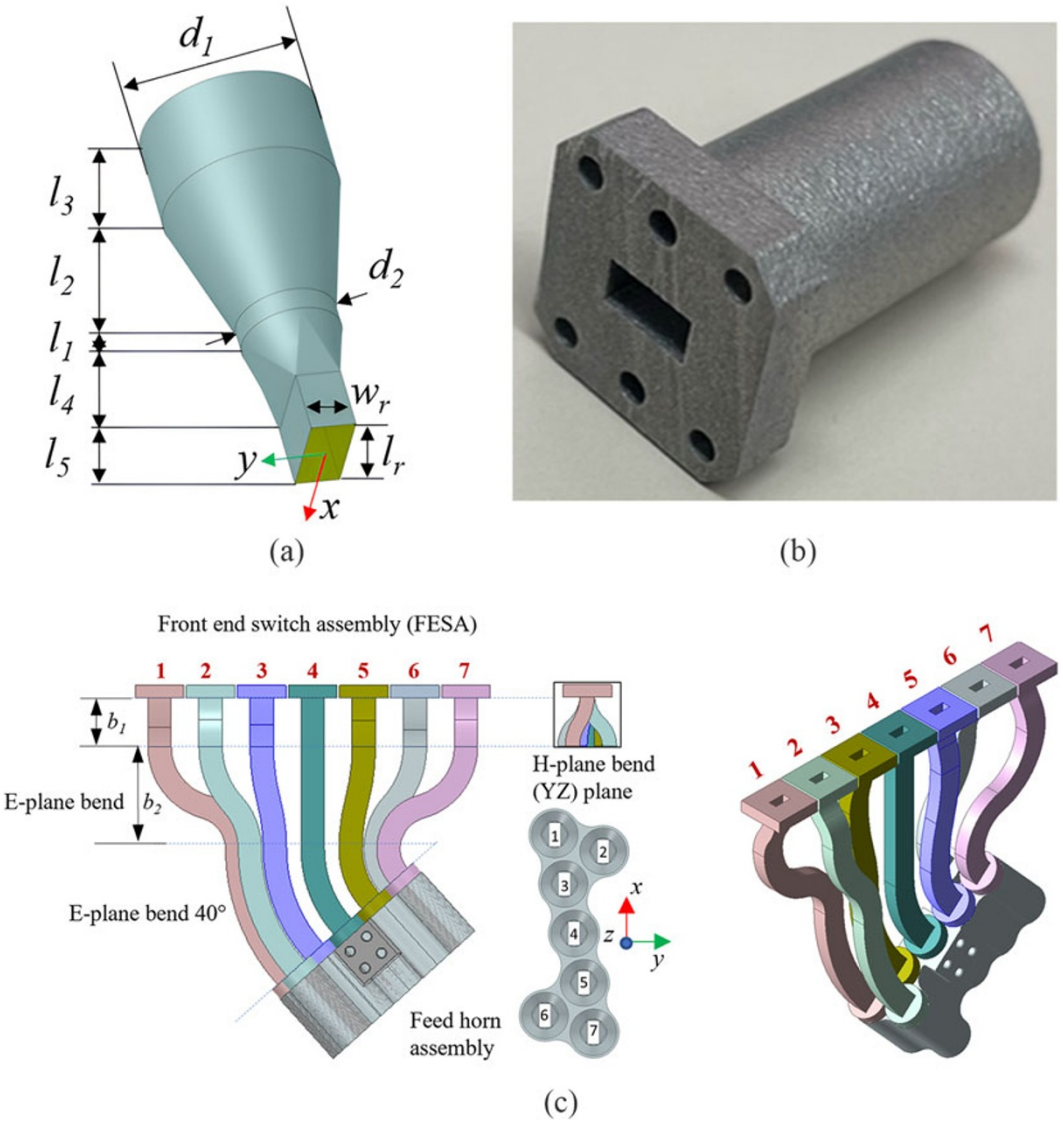


Figure 5. Feed assembly model with seven ports and feeding network. (a) Single horn interior profile, (b) single horn fabricated prototype, (c) seven-horn cluster arrangement and feeding network.

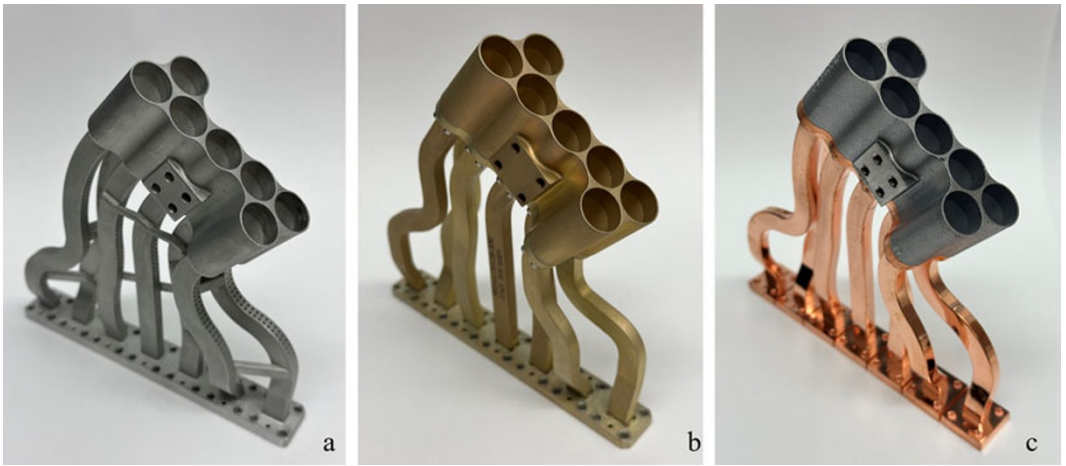


Figure 6. Fabricated feed assembly prototypes. (a) Golden Devices prototype (hybrid additive manufacturing and casting aluminum), (b) Frontgrade Technologies prototype (standard machining aluminum and standard tooling for aluminum waveguide), (c) Custom Microwave Inc. Prototype (aluminum metal additive manufacturing for horns and standard tooling for copper waveguides).

https://doi.org/10.1017/S1759078725000364 Published online by Cambridge University Press

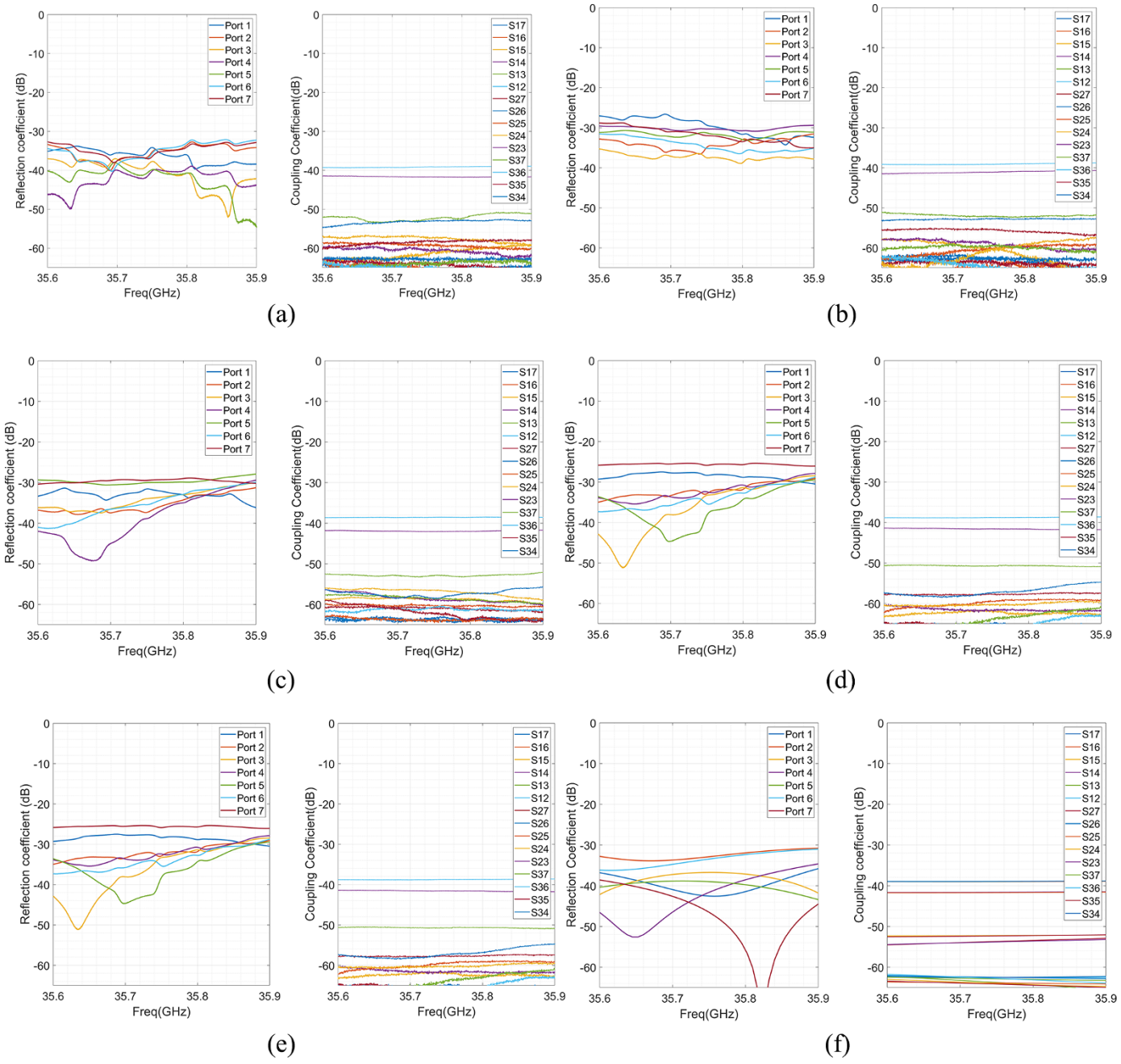


Figure 7. Reflection and coupling coefficients for different prototypes. (a) Golden Devices SLA copper prototype, (b) Golden Devices aluminum cast prototype, (c) CMI doubly-curved rectangular-to-circular transition, (d) CMI linear rectangular-to-circular transition, (e) Frontgrade prototype, (f) simulation results from Ansys HFSS.

Frontgrade Technologies used a different approach, machining the horn assembly from a block of Aluminum 6061. This process only allows for a linear rectangular-to-circular transition to be manufactured in a single piece. In our studies, when comparing the performance of a doubly curved transition with a linear transition, the former was found to provide a better return loss. Standard machined aluminum horns were chosen to provide an additional option, in case the additive manufacturing process could not provide the desired surface accuracy and performance. In this case, (shown in Fig. 6(b)) the feeding network was also made with standard Aluminum 6061 waveguides and dip-brazed flanges. The overall mass for this prototype is 167 g.

Custom Microwave Inc. (CMI) used metal additive manufacturing to produce the horn assembly with the Aluminum alloy AlSi10Mg. Prototypes with both doubly curved transition and linear transition were manufactured to compare their measured performance. The feeding waveguides were manufactured with copper using traditional methods, involving bending the pipes with tooling, and soldering the flanges using Sn96 (prototype shown in Fig. 6(c)). The mass of the prototype is 372 g. Their waveguide assembly manufacturing technique has been used to

https://doi.org/10.1017/S1759078725000364 Published online by Cambridge University Press

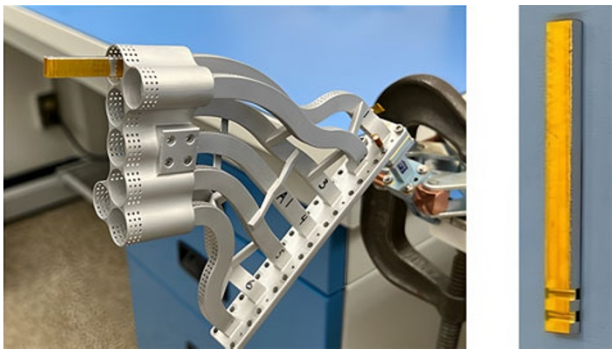


Figure 8. Waveguide insertion loss measurement set-up for Golden Devices prototype using shorting tool. Shorting tool is shown on right.

develop numerous space-qualified parts over the years, and is thus well standardized.

Based on the thermal environment and a sensitivity analysis for the feed assembly, all the prototypes built using these three methods can withstand temperature variations and maintain a solid RF performance during the mission. By exploring these different manufacturing processes and techniques we could evaluate the best solution for INCUS and ensure accurate and reliable performance from the RF, structural and thermal perspective.

Feed assembly measurements

The RF performance of several prototypes made using the three different methods discussed above was measured at JPL, yielding excellent results that met all our major requirements. Figure 7 shows the reflection and coupling coefficients for all seven ports for both measured and calculated results. For Golden Devices prototypes it can be observed that both copper-plated Polyimide prototypes and cast Aluminum prototypes have reflection coefficients below −27 dB and coupling between ports starting at −37 dB or better. These results align well with the calculated values across the band of interest, centered around 35.755 GHz. For CMI prototypes, the reflection coefficients for doubly curved and linear rectangular-to-circular transitions are below −29 dB and −25 dB, respectively. The highest coupling is observed between ports 1–2, and 6–7, which are positioned closer together in the E-field direction. Both reflection and coupling coefficients from CMI prototypes compare well with computed values. The prototype from Frontgrade presented a reflection coefficient that did not meet a −27 dB requirement and was therefore not subjected to further testing.

To measure the insertion loss of the waveguides for the Golden Devices prototypes, a specialized tool was designed to short the waveguide at the throat of the horn. The other end of the waveguide was connected to the PNA and the loss was measured using the reflection method, then divided by 2 to account for the doubled path length. The measurement setup and the shorting tool are shown in Fig. 8. This method was first validated using a 101.6 mm (4″) straight waveguide section by comparing the results with the insertion loss measured using the S21 method. For CMI prototypes, where the waveguide and horn sections have been built separately, a simple shorting plate was placed on the horn side of the waveguide, and the insertion loss was measured using the reflection method. The measured insertion loss values for different prototypes are presented in Table 1.

Retro-simulations were done with an effective/equivalent conductivity and a surface roughness model for verifying the measured losses. The waveguides have been assigned finite conductivity boundary condition in HFSS with user defined conductivity and surface roughness value. The conductivity for CMI copper waveguides has been taken as 5.8×10^7 Siemens/m, and the surface roughness was found to be 0.3 μm to closely resemble the measured performance. In case of cast aluminum waveguides from Golden Devices, the effective conductivity and surface roughness for best fit with measured results was estimated as 2.2×10^7 Siemens/m and 4 μm, respectively. These values correspond closely with the conductivity of aluminum alloy Peraluman 30, and the casting process surface roughness estimates from the manufacturer. As expected, the CMI copper parts have better insertion loss values compared to the cast aluminum parts from Golden Devices. However, the copper-plated polyimide parts from Golden Devices show comparable insertion loss with the CMI part. Aluminum cast prototypes from Golden Devices have slightly higher insertion loss than copper-plated prototypes, as anticipated, however, still performed better than the project requirements, confirming that the surface accuracy and roughness of the hardware is sufficient for this application. The insertion loss for the single horns fabricated at JPL using additive manufacturing with aluminum alloy was measured separately, both by shorting the horn with a plate and measuring two single horns back-to-back. Both methods produced consistent and repeatable results, with an insertion loss of 0.03 dB for the horn, likely conservative, since the horn also includes a 5 mm waveguide section. When combining the horn and waveguide loss together, the worst-case insertion loss for feed assembly is better than 0.25 dB.

Table 1. Insertion loss (dB) at 35.755 GHz for different prototypes waveguides

Insertion loss at 35.755 GHz (dB)	Golden Devices SLA copper plated waveguide (measured)	Golden Devices Cast aluminum waveguide (measured)	Golden Devices Cast aluminum waveguide (simulated)	CMI copper WG (measured)	CMI copper WG (simulated)
Port 1	0.11	0.21	0.22	0.11	0.12
Port 2	0.10	0.20	0.21	0.10	0.11
Port 3	0.11	0.17	0.18	0.09	0.09
Port 4	0.11	0.15	0.16	0.09	0.08
Port 5	0.09	0.14	0.15	0.07	0.08
Port 6	0.08	0.15	0.15	0.08	0.08
Port 7	0.08	0.18	0.16	0.09	0.09

https://doi.org/10.1017/S1759078725000364 Published online by Cambridge University Press

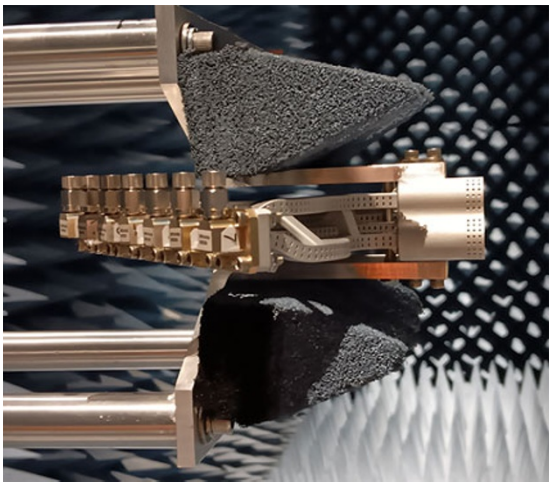


Figure 9. Radiation pattern measurements test set up for feed assembly.

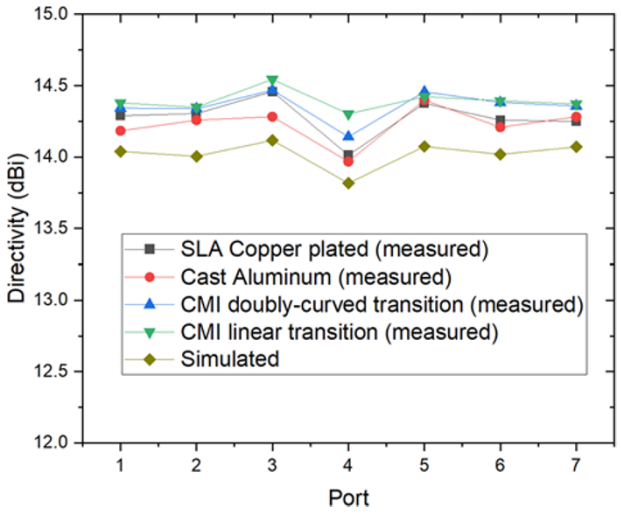


Figure 10. Directivity comparison for different prototypes at 35.755 GHz.

Radiation patterns for the prototypes were measured using a near field spherical antenna range. Laser metrology was employed to characterize the alignment of the center of the feed assembly with the reference coordinate system of the measurement range. The measurement setup is illustrated in Fig. 9. The measured and computed directivity values are shown in Fig. 10. Representative normalized radiation patterns for Port 1 and Port 4 at phi = 0° and 90° cuts are presented in Figs. 11 and 12. Figure 11 compares the Golden Devices copper-plated and cast aluminum prototypes with the computed results, and Fig. 12 compares the CMI prototypes with doubly curved rectangular-to-circular waveguide transition with the computed results. The 3 dB beamwidth for feed horns is 33° and 40° for 0° and 90° cuts, respectively.

During measurements, it was observed that the directivity for the center horn #4 was slightly lower than the other horns, as seen in Fig. 10. Additionally, the measured radiation pattern for the center horn #4 exhibited small irregularities, or "bumps" in the 90° cut around the peak of the main lobe as compared to the side horns. The issue was traced back to the preliminary GSE flange used to mount the assemblies on the range positioner, which prevented the effective coverage of the top part of GSE with absorber (visible in Fig. 9). Consequently, an RF model mimicking the as-mounted configuration was created, which shows excellent agreement with the measured data as shown in Figs. 11 and 12. The bumps or ringing in the main lobe were thus attributed to reflections from the mounting flange and are not visible in the results for Port 1. Remarkably, the measured radiation patterns show excellent agreement with the computed results for both co-polarization and cross-polarization up to about 120° off-boresight angles in either direction. The back lobe, however, was not measured accurately due to the absorber on the spherical range positioner. It is also important to note that the subtended angle of the reflector is only ±34°, and within this region, the agreement between the measured and computed patterns is particularly strong. The cross-polar isolation is better than 25 dB in the subtended angle range of the reflector. The measured directivity values are slightly higher than the computed values, as shown in Fig. 10. The absence of a back lobe in the measured data also contributes to this difference. By removing the back-lobe data beyond 120° from the computed data and recomputing the directivity, the gap was reduced by approximately 0.15 dB. The measured radiation patterns of the designed horn antenna are ultimately used to illuminate the 1.6 m reflector and calculate the overall performance of the antenna.

Based on the measurement results, the RF performance of both the cast aluminum prototype from Golden Devices and the additively manufactured horn and copper waveguides from CMI meet the mission requirements. However, due to the manufacturability of the cast Aluminum prototype in a single piece leading to the removal of the interface, alignment pins and fasteners, and in turn, the reduction of mass, it was decided to use this manufacturing process for the flight hardware. Some modifications were done to the design mostly based on feedback from the structural analysis, and they are discussed in detail in the following section.

Modified feed assembly

A structural analysis was done on the antenna feed assembly based on the expected launch loads to assess the structural integrity and the most critical mechanical resonance modes. This analysis utilized the documented tensile strength and fatigue of the Peraluman 30 alloy. Based on the feedback from this analysis, the mechanical design of the antenna assembly was modified to further enhance the strength of the structure. The modified feed assembly is shown in Fig. 13. Key structural improvements are mentioned as follows. Larger fillets have been included at the joints, particularly around the FESA interface, to provide better structural support. The waveguides are reinforced with larger bracing, which not only strengthens the structure but also facilitates material flow between the waveguides during the casting process. Ribs are added to both wide and slotted sides of the waveguides. Venting holes have also been incorporated to allow for outgassing at the FESA interface. The thickness of the horn wall is increased to 1 mm for enhanced structural strength, though, the thickness at the aperture lip is maintained to preserve the radiation performance. The outer wall of the horn is also tapered down towards the lower end, rather than staying cylindrical as in the previous version, which also offsets the additional mass. This also results in a more uniform cooling throughout the structure during the casting process, and in turn, delivers more consistent material properties throughout the structure. It is notable that the entire feed assembly weighs only 126 g.

https://doi.org/10.1017/S1759078725000364 Published online by Cambridge University Press

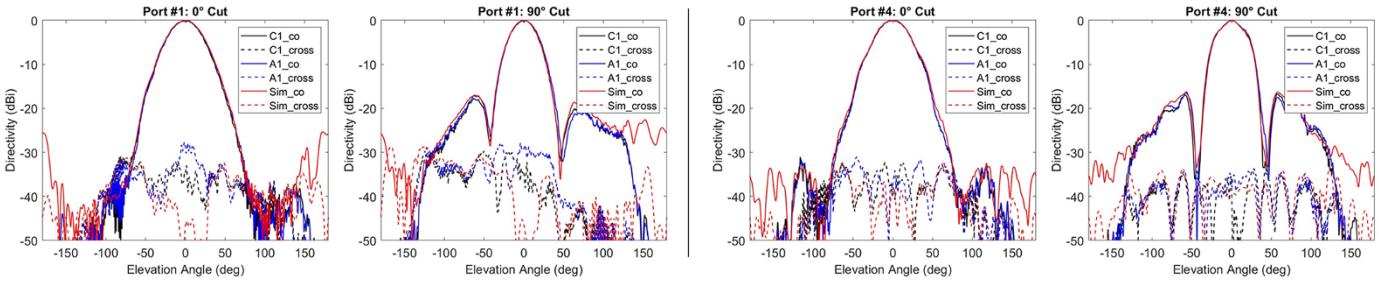


Figure 11. Measured and calculated normalized radiation patterns for Golden Devices prototypes port 1 and port 4 on 0°, 90° cuts for co-pol and cx-pol. C1 are measured results from a copper-plated polyimide assembly (black), A1 are measured results from a cast aluminum assembly (blue). Simulations are in red.

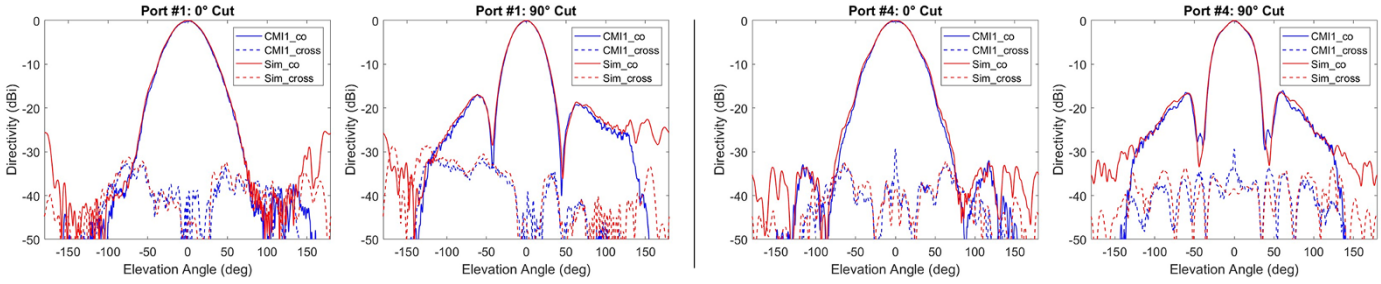


Figure 12. Measured and calculated normalized radiation patterns for CMI prototypes with doubly-curved rectangular-to-circular waveguide transition. Port 1 and port 4 on 0°, 90° cuts for co-pol and cx-pol. CMI1 are measured results for assembly (blue). Simulations are in red.

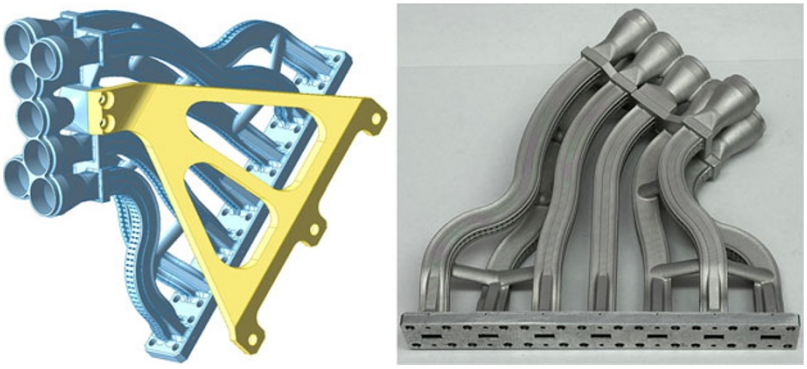


Figure 13. Modified antenna feed assembly.

With the maturation of the radar assembly, a single bracket is now used to support the feed. Based on the previous observations of the radiation patterns anomaly, we anticipated similar issues due to the reflection from the top face of the metallic flange used to mount the feed assembly. To mitigate these reflections, the attachment point of the flange is lowered below the neck of the horn, and the top face is chamfered at 45° angle as shown in Fig. 13. The antenna assembly is fabricated using the hybrid additive manufacturing and casting process, achieving a surface roughness better than 5μm and surface accuracy better than 20μm. A complete fabricated prototype of the modified model is also shown in Fig. 13.

The feed assembly is measured for all S-parameters for the 7 ports and the results are presented in Fig. 14. A reflection coefficient better than −27dB and a coupling coefficient better than −38dB is obtained in the band of operation. The highest coupling is observed between ports 1–2, and 6–7, which are positioned closer together in the E-field direction. The insertion loss is better than 0.25dB including the loss due to both the horn assembly and the feeding waveguides. The radiation patterns were measured using the same process, however, the GSE bracket to mount the feed assembly in the spherical range was replaced by the bracket designed along with the feed, which will be used to mount the feed assembly on the spacecraft. The normalized radiation patterns show a very good match with the simulated results except for the back-lobe where the antenna and the positioner were covered with absorber (Fig. 15). The measured directivity for the horns ranged between 14.1 dBi and 14.3 dBi, and the reduction in directivity for center horn #4 for the previous prototypes was not observed anymore, similarly to the bumps in the radiation pattern for Port 4. The measurements were also repeated with the feed covered with aluminum foil, with the intent of simulating a multi-layer insulation (MLI) blanket, as the feed assembly will be covered with thermal blankets during flight to limit temperature swings during operations. It was observed that the presence of MLI blanket did not affect the radiation patterns and the directivity of the antenna feed assembly.

https://doi.org/10.1017/S1759078725000364 Published online by Cambridge University Press

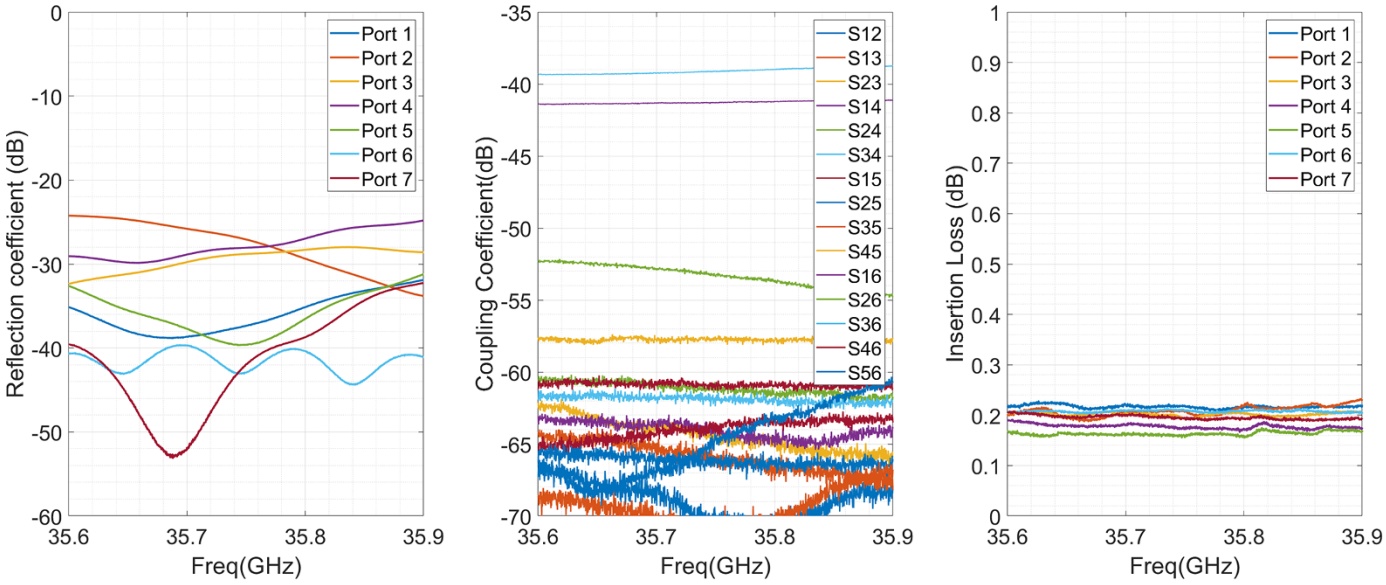


Figure 14. Measured S-parameters for the modified feed assembly.

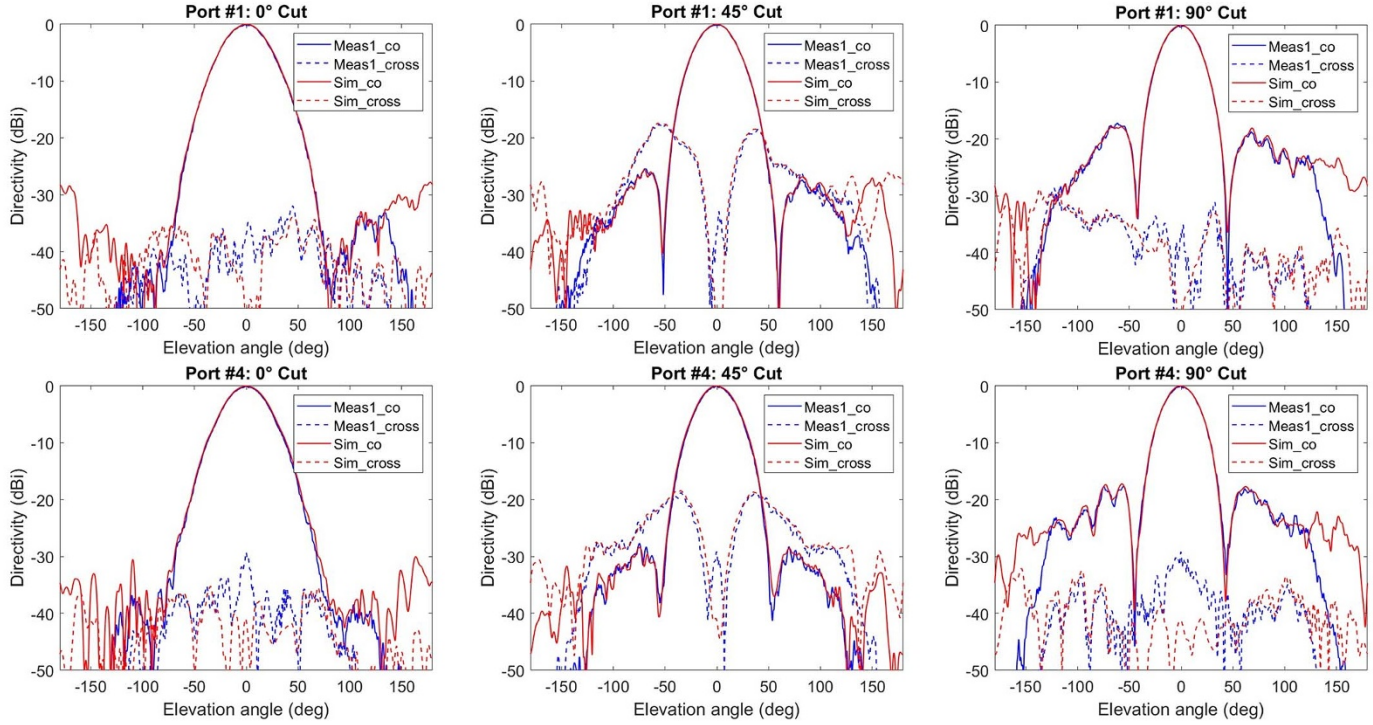


Figure 15. Measured and calculated normalized radiation patterns for modified feed assembly for port 1 and port 4 on 0, 45, and 90 cuts for co-pol and cx-pol.

Conclusion

This paper presented the seven-horn cluster feed assembly for the 1.6 m mesh reflector antenna for INCUS DAR. To provide spatial redundancy and relax the pointing requirements between the three identical satellites, the feed assembly cluster provides seven secondary beams with 2/3 of the 3 dB beam overlap. This requires the horns to be kept closer than the standard WR28 flange dimensions, and thus a custom waveguide feed network has been designed to interface with the 8-port FESA. In this paper, we described and compared the design and fabrication approaches for the development of the feed assembly for INCUS and its RF, mechanical, and structural performance. The hardware fabricated by Golden Devices and CMI was tested with excellent results. Based on the feedback from the radiation pattern measurements and the structural analysis, the feed assembly was structurally modified to survive launch loads and improve the casting process to obtain consistent material properties in the structure. The feed assembly meets the mission RF requirements over the band of operation, including the reflection and coupling coefficients at the input ports, insertion loss of the horns and waveguides, directivity

https://doi.org/10.1017/S1759078725000364 Published online by Cambridge University Press

and beamwidth to illuminate the reflector, and maintaining performance over temperature. The measured radiation patterns from the feed assembly are used to illuminate the mesh reflector which results in high-efficiency secondary beams to measure reflectivity profiles from clouds over the tropical region and the CMF.

Data availability statement. The data that support the findings of this study are available from the corresponding author upon reasonable request.

Acknowledgements. This work was carried out at the Jet Propulsion Laboratory, California Institute of Technology, under a contract with the National Aeronautics and Space Administration. © 2024 California Institute of Technology. Government sponsorship acknowledged. Reference herein to any specific commercial product, process, or service by trade name, trademark, manufacturer, or otherwise, does not constitute or imply its endorsement by the United States Government or the Jet Propulsion Laboratory, California Institute of Technology. The authors would like to thank Jefferson Harrell, Tom Musselman and Nakul Mohakar for their help in the analysis and measurements.

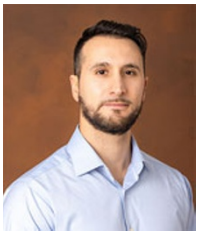
Competing interests. The authors report no conflict of interest.

References

1. **NASA Press Release** (2021) NASA Selects New Mission to Study Storms, Impacts on Climate Models, 5 November 2021. https://www.nasa.gov/press-release/nasa-selects-new-mission-to-study-storms-impacts-on-climate-models.
2. **Freebury GE and Beidleman NJ** (2016) Deployable Reflector. U.S. Patent 2017222308, 28 January 2016.
3. **Peral E, Imken T, Sauder J, Statham S, Tanelli S, Price D and Chahat N** (2017) RainCube, a Ka-band Precipitation Radar in a 6U CubeSat. In *31st Annual AIAA/USU Conference on Small Satellites*, August 2017.
4. **Chahat N, Sauder J, Babuscia A, and Thomson M** (2021) *Radar in a Cubesat: RainCube, CubeSat Antenna Design*. NJ, USA: Wiley-IEEE Press, pp. 91–138, ch3.
5. **Reising S, Gaier TC, Kummerow C, Padmanabhan S, Lim BH, Heneghan C, Chandrasekar V, Olson JP, Brown ST, Carvo J and Pallas M** (2017) Temporal Experiment for Storms and Tropical Systems Technology Demonstration (TEMPEST-D) Mission: Enabling time-resolved cloud and precipitation observations from 6U-class satellite constellations. *31st AIAA/USU Conference on Small Satellites*, August 2017.
6. **Boudad K and Kostelecky Q** (2023) Relative Phasing and Observations Overlap: Low-Thrust Trajectory Design Options for INCUS Mission, In *AAS/AIAA Space Flight Mechanics Meeting*, Austin.
7. **Dolan B, Kollias P, van den Heever SC, Rasmussen KL, Oue M, Luke E, Lamer K, Terserras BP, Haddad Z, Stephens G and Chandrasekar V** (2023) Time resolved reflectivity measurements of convective clouds. *Geophysical Research Letters* **50**(22), e2023GL105723. doi:10.1029/2023GL105723
8. **Rao SK, Tang M, and Hsu C** (2006) Multiple beam antenna technology for satellite communication payloads. *ACES Journal* **21**(3), 353–364.
9. **Gupta G and Focardi P** (2024) Feed assembly development for INCUS. In *Proceedings of the 18th European Conference on Antennas and Propagation*, Glasgow, UK, 17–26 March 2024.
10. **Mancini A, Chahat N, Tanelli S and Focardi P** (2023) A Multi-Beam Ka-Band Deployable Mesh Reflector Antenna for the INCUS Mission. In *Proceedings of the 17th European Conference on Antennas and Propagation*, Florence, Italy, 26–31 March 2023.
11. **Gupta G, Mancini A and Focardi P** (2023) Preliminary feed assembly design for INCUS. In *Proceedings of Wireless, Antennas and Microwave Symposium*, Gandhinagar, India, 7–10 June 2023.
12. **Gupta G and Focardi P** (2024) Horn feed assembly modification for INCUS. In *Wireless, antennas and microwave symposium, India*, March 2024.
13. https://www.ticra.com/software/champ3d/



Gaurangi Gupta received a M.Tech. and Ph.D in Electrical Engineering from the Indian Institute of Technology Kanpur, India, in 2014 and 2020, respectively. She was a post-doctoral researcher at NASA Jet Propulsion Laboratory, Caltech, USA from 2021 to 2022, where she is currently working as an RF Microwave Engineer. Her research interests include antenna modelling and characterization, satellite antennas, antenna arrays, and metasurface.



Alessio Mancini received a B.S. and a M.S. in Engineering of the Telecommunications from the University of Bologna in 2007 and 2011, respectively and Ph.D. in Electrical Engineering from the University of Oklahoma, Norman in 2018. He is currently working for JPL as RF Microwave Engineer for the MSR-SRL program. He is also working in the Envision-VenSAR and the INCUS missions. His areas of specialization are wet radome characterization, antenna theory, and electromagnetic modeling.



Paolo Focardi is a Group Lead for Technology Development at NASA Jet Propulsion Laboratory, California Institute of Technology. He's also the chair of the IEEE Antennas and Propagation Society chapter of the Coastal Los Angeles Section. He received a PhD in Computer Science and Telecommunication Engineering from the University of Florence, Italy, in 2002. He has been at JPL with various responsibilities since 1999 working on a variety of R&D and flight project including SRTM, Aquarius, JUNO, SMAP, COWVR, NISAR, INCUS, and VERITAS. His work is focused on analytical and numerical methods in electromagnetism for the analysis and design of RF circuits and antennas. He's been leading the implementation of extremely complex and detailed RF models capable of predicting the performance of large instruments with unprecedented accuracy. Currently he is exploring how the latest additive manufacturing techniques can be used effectively for flight projects. He has authored and co-authored over 80 journal and conference publications including two book chapters about reflector antennas.

https://doi.org/10.1017/S1759078725000364 Published online by Cambridge University Press